Naya, F., González, C., Lopes, C., van der Veen, S. & Pons, F. (2017). Computational micromechanics of the transverse and shear behavior of unidirectional fiber reinforced polymers including environmental effects. *Composites Part A: Applied Science and Manufacturing, 92*, 146–157.

DOI: 10.1016/j.compositesa.2016.06.018

# Computational micromechanics of the transverse and shear behaviour of unidirectional fiber reinforced polymers including environmental effects

F. Naya[a], C. González[a,b,*], C.S. Lopes[a], S. Van der Veen[c], F. Pons[c]

[a] *IMDEA Materials Institute, C/Eric Kandel, 2, 28906 Getafe, Madrid, Spain*
[b] *Department of Materials Science, Polytechnic University of Madrid, ETS de Ingenieros de Caminos, 28040 Madrid, Spain*
[c] *AIRBUS Structures Research and Integration, ESIRNM. 18 rue Marius Terce, 31300 Toulouse, France*

**Abstract**

Qualification of Fiber Reinforced Polymer materials (FRP's) for manufacturing of structural components in the aerospace industry is usually associated with extensive and costly experimental campaigns. The burden of testing is immense and materials should be characterized under different loading states (tension, compression, shear) and environmental conditions (temperature, humidity) to probe their structural integrity during service life. Recent developments in multiscale simulation, together with increased computational power and improvements in modeling tools, can be used to alleviate this scenario. In this work, high-fidelity simulations of the material behaviour at the micro level are used to predict ply properties and ascertain the effect of ply constituents and microstructure on the homogenized ply behaviour. This approach relies on the numerical analysis of representative volume elements equipped with physical models of the ply constituents. Its main feature is the ability to provide fast predictions of ply stiffness and strength properties for different environmental conditions of temperature and humidity, in agreement with the experimental results, showing the potential to reduce the time and costs required for material screening and characterization.

*Keywords:* A. Polymer-matrix composites (PMCs), C. Multiscale modelling, C. Finite element analysis(FEA), C. Computational micromechanics

## 1. Introduction

Fiber Reinforced Polymers (FRPs) are nowadays extensively used in applications where good mechanical properties are required in combination with weight savings. However, despite all existing information and current knowledge about these materials, the accurate prediction of the failure

*Corresponding author
*Email address:* carlosdaniel.gonzalez@imdea.org (C. González)

stress of composite materials and structures has been an elusive task due to the complexity of the failure mechanisms involved.

Various phenomenological and physically-based models have been proposed, whose input parameters have to be obtained through costly and time-consuming experimental campaigns for each material system. [1, 2]. Results obtained for a given unidirectional FRP system can not be directly extrapolated directly to other configurations with different fibre volume fraction or constituent properties, leading to a massive investment for their physical characterization. This is the case of material qualification for the aeronautical industry, where the whole process can last well over two years due to the required tests under different ageing and environmental conditions.

Computational micromechanics (based on Finite Elements Analysis) offers a novel approach to understand the deformation and fracture mechanisms in materials engineering. In the case of unidirectional fibre-reinforced composites, it has demonstrated high accuracy in the prediction of the mechanical behaviour, including fracture mechanisms under complex multiaxial loading cases [3–5]. Numerical simulations of Representative Volume Elements (RVE's) of the composite microstructure are useful to predict homogenized lamina properties, in close agreement with experimental data [6], and to provide the necessary input data for mesomechanical analysis at the laminate level. This bottom-up multi-scale simulation approach might lead in the future to a drastic reduction of the current costs associated with properties screening and material characterization programs [7]. In addition, computational simulation of micromechanical RVE's can be used to reproduce experimental stress conditions rather difficult to impose experimentally in laboratory, such as biaxial or triaxial stress states. Moreover, the influence of the microstructure and the constituents properties in the failure mechanisms can be addressed by means of parametric studies. All these efforts can lead in the future to the development micromechanical-based failure criteria with physical soundness, a clear advance in the state-of-the-art, e.g. Puck [8], LaRC [9] and Catalanotti [10] models.

Following previous research works [11, 12], herein detailed information of the microstructure (fiber diameter distribution, volume fraction, fiber clusters and resin pockets) is captured and included in a computational model of a unidirectional lamina (UD). Several strategies to determine micromechanical parameters by fitting against experimental results at the ply level, rather than measuring them with independent tests at the micro level, were developed in the past [13, 14]. In this work, the behavior of the constituents is obtained from micromechanical experiments on the material constituents performed under different environmental conditions. The measured properties are inputs of the constitutive equations of matrix and fiber/matrix interfaces. The RVE is submitted

to homogeneous stress states to determine the material failure envelope in the $\sigma_{22} - \tau_{12}$ plane under different environmental conditions, including the pure mode ply strengths, namely transverse tension strength ($Y_T$), transverse compression strength ($Y_C$), and longitudinal shear strength ($S_L$). The model shows the importance of capturing adequately the competition between the different failure mechanisms, fiber/matrix debonding and matrix failure, operating at the same time when the material is subjected to mechanical and environmental loads.

This introduction is followed by the description of the computational micromechanics framework, i.e. of the constitutive equations used to simulate matrix, fiber and interfaces, as well of the RVE generation procedure and the subsequent construction of the FE models with the specific loading conditions. The procedures used to characterize the basic ply constituents and model input parameters are explained then. The results of the uniaxial and biaxial loading simulations performed on the Hexcel carbon/epoxy AS4/8552 material (fibre volume fraction: 60% ; cured ply thickness: $0.184mm$) are presented and compared with experimental results. The main advantage of selecting this well-known pre-impregnated material system system is that most of its ply properties are directly provided by prepreg manufacturer or found in the literature since it has been widely used in the aeronautical industry and subject of research, e.g. [15, 16].

The experimental-computational approach presented in this work constitutes an good complement to the experimental characterization campaigns of composite materials to reduce time and costs associated and providing fast screening capabilities to improve material downselection for a given engineering application.

## 2. Computational micromechanics model

### *2.1. RVE model set-up and simulation*

Computational micromechanics is based on the analysis of a statistically representative volume element of the material (RVE) subjected to homogeneous stress states (tension, compression and shear) or temperature increments. The microstructure of the RVE of the unidirectional composite is idealized as a dispersion of parallel and circular fibers randomly dispersed in the polymer matrix. A total number of fibers around 50 is enough to capture adequately the essential features of the microstructure of the material [17] while maintaining reasonable computing efforts. Synthetic fiber distributions statistically equivalent to the real ones are generated for the analysis. To this end, several strategies are available in the literature [12, 18, 19] being the Random Sequential Adsorption (RSA) algorithm [11], probably, the most popular due to the easiness to achieve large volume

fraction of fiber reinforcement. In this work, the RSA algorithm was compared with the Nearest Neighbor Algorithm (NNA) developed by Vaughan and McCarty [12] using the relevant microstructure statistical information obtained from micrographs of the unidirectional ply cross section. As shown in Figure 1, the results revealed well-distributed fiber microstructures without significant fiber clustering or matrix rich regions. Hence, it can be concluded that both algorithms deliver similar microstructures.

Considering its reliability and computing speed, the RSA algorithm was preferred in this work. Two-dimensional periodic fiber distributions were generated with the RSA algorithm and extruded along the fiber direction to achieve the final RVE's of the unidirectional composite material. The periodic RVE's were then discretized using isoparametric wedge and brick finite elements for fibers and matrix with full integration at Gauss points (C3D6 and C3D8, respectively, in Abaqus [20]). Typically, each RVE contains approximately $\approx 40000$ elements representing a discretization fine enough to capture the large stress gradients between neighboring fibers. Node positions on opposite faces of the RVE's are identical in order to apply periodic boundary conditions according to the methodology developed by Segurado and LLorca [11]. Simulations were carried out with Abaqus/Standard within the framework of the finite deformations theory with the initial unstressed state as reference.

The RVE's were initially subjected to a homogeneous temperature drop of $\Delta T = -160^oC$ from the curing ($180^oC$) to room temperature ($20^oC$), hence generating realistic residual stress states in the material before mechanical loading. In a second step, homogeneous stress states were introduced by applying the appropriate displacements to the master nodes linked with the periodic boundary conditions [17]. The displacement and reactions of these master nodes were used to determine the stress-strain curves under transverse, shear and combined loads, and to derive the corresponding material stiffness and strength properties.

[Figure 1 about here.]

### *2.2. Constitutive equations*

Carbon fibers are modeled in this work as linear, elastic and transversally isotropic solids. The anisotropy is taken into account by defining five independent elastic constants ($E_{f1}, E_{f2}, \nu_{f12}, G_{f12}, G_{f23}$) and two different thermal expansion coefficients ($\alpha_{f1}, \alpha_{f2}$).

The polymer matrix of the composite material is simulated as an isotropic linear and elastic solid with $E_m$ and $\nu_m$ as elastic modulus and Poisson ratio. In addition, the matrix is able to undergo plastic deformations with the possibility of damage by cracking under tensile loads. This

approach has been adopted by other researchers in the literature [14, 21–23] as it represents a realistic behavior of a polymer [24]. The damage-plasticity model, available in ABAQUS/Standard [20] and schematically illustrated in Figure 2, is a modification of the Drucker-Prager plasticity yield surface [25] by including a damage variable in order to capture the quasi-brittle behaviour of the polymer under dominant tensile loads. The constitutive equation is based on the yield function proposed by Lubliner et al. [26] including modifications proposed by Lee and Fenves [27] to account for strength evolution under tension and compressive loads. The yield function defined in terms of the $I_1$ and $J_2$ invariants of the stress tensor is

$$\Phi(I_1, J_2, \sigma_I, \beta, \alpha) = \frac{1}{1-\alpha}\left(\sqrt{3J_2} + \alpha I_1 + B\langle\sigma_I\rangle\right) - \sigma_{myc} = 0 \tag{1}$$

wherein $I_1$ stands for the first invariant of the stress tensor, $J_2$ is the second invariant of the deviatoric stress tensor, $\alpha$ is the pressure-sensitivity parameter of the Drucker-Prager yield criterion, $\sigma_I$ is the maximum principal stress, $\langle\ \rangle$ the Macaulay brackets (returning the argument if positive and zero otherwise) and $B$ is a function of the tensile and compressive yield stresses, $\sigma_{myt}$ and $\sigma_{myc}$, defined as

$$B = \frac{\sigma_{myt}}{\sigma_{myc}}(1-\alpha) - (1+\alpha) \tag{2}$$

Under biaxial compression stress state, with $\sigma_I = 0$, equation 1 reduces to the initially proposed Drucker-Prager yield condition [25], wherein $\alpha$ can be expressed in terms of the internal friction angle of the material ($\beta$) according to $\tan\beta = 3\alpha$. The internal friction angle controls the hydrostatic pressure dependence of the plastic behaviour of the material. Simultaneously, $\alpha$ can be related to the biaxial compression behavior according to

$$\alpha = \frac{\sigma_{b0} - \sigma_{c0}}{2\sigma_{b0} - \sigma_{c0}} \tag{3}$$

After the onset of damage in tension at $\sigma_{tm}$, the softening behavior is controlled by an exponential cohesive law, characterized by a single normalized scalar damage variable, to ensure the correct energy dissipation of the matrix $G_m$. More details about the constitutive model and the numerical implementation can be found in [20, 28].

[Figure 2 about here.]

Even though this damaged-plasticity model requires a complex calibration from detailed experiments, good results can be obtained by the assumption of default parameters while measuring the

key properties. An experimental micromechanics approach, to be fully detailed in the following section, was developed in by [29] to determine the Young modulus $E_m$, the compression yield limit $\sigma_{myc}$ and the internal friction angle $\beta$ of amorphous polymers by means of indentation.

Fiber-matrix debonding is modelled by means of a surface-based cohesive interaction, ABAQUS/Standard [20]. The cohesive constitutive equation relates the displacement jump across the interface to the traction vector acting on it for cracking under the full range of mode-mixities as in [30]. The initial response of the cohesive interaction is assumed to be linear elastic governed by a contact penalty stiffness $K$. Such numerical parameter should be large enough to ensure displacement continuity in the absence of interface damage while avoiding convergence difficulties due to ill-conditioned stiffness matrix. Damage onset is controlled by a quadratic interaction criterion depending on the fibre/matrix interface strength (normal - $\sigma_n$, shear transversal - $\tau_T$, and shear longitudinal - $\tau_L$), as

$$\left(\frac{\langle\sigma_n\rangle}{\sigma_n^0}\right)^2+\left(\frac{\tau_T}{\tau_T^0}\right)^2+\left(\frac{\tau_L}{\tau_L^0}\right)^2=1 \tag{4}$$

wherein only positive normal tractions affect the criterion. Once fiber/matrix debonding is initiated, the cohesive tractions transferred through the interface decrease linearly to zero by means of a single normalized scalar damage variable. The energy-based Benzeggagh-Kenane (BK) damage propagation criterion [31] is used to account for the fracture energy dependence on the mode mixity as

$$G_c=G_{Ic}+(G_{IIc}-G_{Ic})\left(\frac{G_{shear}}{G_I+G_{shear}}\right)^m \tag{5}$$

Cohesive interactions were used in the model to include the effect of friction occurring after fiber/matrix debonding. The shear stresses caused by friction at the interface are ramped progressively and proportional to the degradation of the interface, and thus, once the fiber/matrix interface is fully debonded, the surface interaction is uniquely governed by a pure Coulomb model. This friction stresses causes an increment of the interface shear resistance proportional to the normal compressive loads applied on it, being $\mu$ the constant of proportionality or friction coefficient. It should be mentioned that this affects not only the post-debonding behavior of the interface but also the cohesive response as the friction stresses are ramped with the interface damage variable, as schematically illustrated in Figure 2.

When using the traditional cohesive elements, instead of the surface-based cohesive approach, friction can only be included when the cohesive element is totally damaged and removed from the finite element mesh. The combined effect of friction with cohesive behavior has been addressed by

other authors, e.g. [32, 33]. These works eventually led to the development of a cohesive element formulation that take both mechanisms into account; a capability similar to the one used in this work with cohesive surface interactions.

## 3. *In-situ* characterization of microconstituents

In order to capture the influence of environmental conditions and manufacturing processes on the ply properties, the constitutive equations include a set of properties measured by means of *in-situ* micromechanical tests that are carried out on the composite coupon. The experimental procedures and results are briefly summarized in this section for the sake of clarity. Additional details can be found in Rodríguez et al. [29, 34].

Carbon fibres are assumed to behave elastically and properties were not dependent on the environmental conditions considered in this work. The longitudinal elastic properties of AS4 fibers at RT/DRY conditions are directly provided by the supplier. The transverse elastic properties and the thermal expansion coefficients were found in the literature [1] or estimated by means of Chamis rule of mixtures [35]. The properties required in the simulations are gathered in Table 1.

[Table 1 about here.]

Matrix and fiber/matrix interface caracterization was carried out using small coupons extracted from an unidirectional AS4/8552 composite laminate. Samples were first cut using a diamond wire and the cross section perpendicular to the fibers polished using diamond slurry down to $1\mu m$ grain size. A typical cross section after polishing is shown in Figure 3. A first set of samples were totally dried in a stove for testing at room temperature conditions (RT/Dry). A second set of samples (HOT/WET) were submitted to aging in environmental chamber at $70^oC$ and 85% of relative humidity. The aging procedure followed the recommendation of DIN EN2823 standard [36] although with small size specimens ($\approx$ 1x1x1 $mm^3$) rather than the standard travelers. The coupon weight uptake was regularly measured until saturation ($\approx$ 3% of the dry weight) was attained which occurred typically after three weeks of humid exposure. It is worth to remark at this point that the use of small size specimens speed up the water uptake process as compared with the typical coupon size used in the usual practice.

[Figure 3 about here.]

### 3.1. Matrix characterization

Nanoindentation experiments were conducted using a Hysitron TI 950 TriboIndenter equipped with a Berkovich tip (pyramidal indenter). A set of approximately 30 indentations were performed for each environmental condition at an equivalent strain rate of $\dot{\epsilon} = 0.07s^{-1}$. The material hardness is computed from the force recorded during the test and the physical imprint introduced in the material. However, determining the real contact area of the material with the indenter is an extremely difficult task as sink-in or pile-up phenomena can mask the results. A first estimation of the real contact area of the indenter is given by Oliver and Phar [37] from the ratio between the total elastic and plastic work ($W_e$ and $W_p$, respectively) measured from the load-displacement curves (see Figure 4). However, there is no analytical method to determine harness from indentations in hydrostatic dependent materials and complex numerical models based on the finite element method should be applied. In this work, the methodology proposed by Rodríguez et al. [29], assuming $\beta = 29^o$ irrespective of the environmental conditions, is used to obtain the elastic modulus and the compressive yields stress of the matrix ($E_m$ and $\sigma_{myc}$, respectively).

[Figure 4 about here.]

The value of the Young modulus of the matrix obtained from nanoindentation in the RT/DRY condition is reported in Table 2 and is in reasonable good agreement with the experimental value provided by the supplier ($E_m = 4.67$ GPa) obtained from macroscopic coupons. The slight differences obtained can be attributed to the constraint effects induced when testing close to fibers. A way to alleviate such effect is by identifying and indenting on wider rich resin pockets or by reducing as much as possible the load applied by the indenter obtaining, therefore, a soft imprint as shown in Figure 3.

Testing under HOT/WET conditions was carried out with a special heating device coupled to the nanoindenter and placed around the Berkovich tip. Specimens were extracted from the environmental chamber ($70^oC$ and 85% of relative humidity) and placed immediately in the Hysitron nanoindentator apparatus. The system was equipped with a heating device and the temperature was controlled and monitored with a thermocouple. The temperature was maintained at $70^oC$ during some minutes. Then, indentations were performed for a limited period of time to avoid drying of the material surface. The properties of the 8552 epoxy resin measured in RT/DRY and HOT/WET conditions are reported in Table 2.

[Table 2 about here.]

The thermal expansion coefficients (CTE) for RT/DRY were obtained from the literature [38]. The mode I fracture toughness of the 8552 resin $G_m$ was not measured in this work. Typical values found in the literature for epoxy resins $G_m$ are in the range of 40 $J/m^2$ and 400 $J/m^2$ depending on crack propagation speed, as reported in [39]. Taking into account this lack of experimental results, a value of fracture energy for the 8552 epoxy matrix $G_m$ in the order of $\approx$100 $J/m^2$ seems to be reasonable in this case [5, 6]. In any case, the simulations demonstrated that the effect of matrix toughness on the transverse and shear strengths of the unidirectional material was limited.

### *3.2. Fiber/matrix interface characterization*

The interface strength was determined using the fibre push-in technique described in [34]. In this test a single fibre is pushed-in by means of a cylindrical flat-tipped nanoindenter until interface debonding occurs. The load-displacement curves of the push-in tests on individual fibers are linear and elastic up to a point where the response deviates from the linearity. This behaviour is attributed to the progressive and stable propagation of a debonding through the fiber/matrix interface. The mechanics of the push-in test were analyzed in detail in [34] by means of detailed FE simulations that allowed the determination of the influence of the different mechanical parameters (interface shear strength, toughness and friction; elastic constants; residual thermal stresses) on the onset of debonding. It should be mentioned that push-in tests only provide the values of the shear strength of the interface along the fiber direction $\tau_L^0$. The normal strength is assumed equal to $\sigma_n^0 = 2/3\tau_L^0$ based on the experimental results obtained by Ogihara and Koyanagi [40] on cruciform E-glass/epoxy specimens subjected to biaxial loading. In addition, in the absence of reliable experimental results, the interface transverse shear strength is assumed equal to the longitudinal one ($\tau_T^0 = \tau_L^0$).

All push-in tests were carried out using a Hysitron TI 950 TriboIndenter equipped with a $5\mu m$ diameter flat punch tip. The indentations were centered as much as possible on the $7\mu m$ AS4 carbon fibers. In order to achieve good reproducibility, fibre push-in tests were performed on the central fibres of highly-packed fibre clusters with hexagonal symmetry, a feature easily found in unidirectional AS4/8552 plies, as shown in Figure 3.

A total of fifteen push-in tests were carried out at RT/DRY and RT/WET conditions. The RT/WET condition was used instead the standard HOT/WET previously used for matrix characterization due to experimental difficulties associated with the thermal stability of the indenter at $70^oC$. The average values, as well as the standard deviation, are gathered in Table 2. It can be observed that the interface strength decreases in the RT/WET condition and this value can be

considered an upper value of the strength of the interface at $70^oC$ and 85% of relative humidity. The additional effect of temperature on the interface strength can be estimated using the knock-down factor on matrix compressive strength due to HOT/WET conditions which can be thought to be entirely due to the temperature increase with respect to RT/DRY conditions. Under this assumption, the HOT/WET matrix compression strength would be further reduced $\approx 17\%$ with respect to a RT/WET environment.

The interface fracture energy in mode I, $G_{Ic}$, could not be measured experimentally but it is assumed to be in the range of $2 - 5J/m^2$. Similar values were used by other authors and reported in the literature [5, 12]. In addition, due to the lack of experimental data, the interface fracture energies in the shear modes were set equal to the matrix cracking fracture energy, $G_{IIc} = G_{IIIc} = G_m = 100J/m^2$, a value similar to the one used in [34]. The fracture energy was assumed to be insensitive to the environmental conditions for the sake of simplicity.

## 4. Micromechanical simulation and model validation

### *4.1. Pure transverse and shear loading*

Under pure transverse tension loading, the fracture process is controlled by the fiber/matrix interface debonding, for both RT/DRY and HOT/WET conditions. Cracks start at the fiber poles along the loading direction in those regions where the stress concentrations in the fiber/matrix interface are higher, for instance in a fiber cluster. After failure of the interface, the matrix undergoes severe plastic deformation, accumulating damage until ultimate failure of the matrix ligaments. The final failure of the RVE is produced by the development of a crack perpendicular to the loading axis, as shown in Figure 5. The behaviour is essentially linear an elastic up to failure being the transverse tension strength of the composite strongly controlled by the fiber/matrix interface strength.

[Figure 5 about here.]

Under pure transverse compression, the final failure of the composite ply takes place by the development of matrix shear bands. However, the fiber/matrix interface plays an important role in the failure initiation process. According to the in-situ nanoindentation tests, the nominal shear strength of the AS4/8552 fiber/matrix interface is lower than the shear strength of the 8552 resin matrix, specially under HOT/WET conditions (see Table 2). If these were the only two mechanisms at play, the simulations show that failure under pure transverse compression would initiate by interface decohesion at the fibre poles and then propagate in the form of a plastic shear band

oriented at $theta_{fr} \approx 47^o$. The introduction of frictional effects in the interaction between fiber and matrix changes this equilibrium between fiber/matrix debonding and matrix shear banding. Friction leads to the increment of the interface shearing resistance due to the normal compressive stresses at the interface generated by the thermal and transverse compressive loadings. For significant values of $\mu$, failure under pure transverse compression appears not to be initiated by interface decohesion but directly by shear banding with orientation $\theta_{fr} \approx 56^o$. This failure mechanism transition effect is represented in Figure 6. Values of shear band orientation similar to the later case were reported in previous research works [41] and are supported by experimental data [42] for similar materials. Therefore, it can be concluded that friction plays an important role in the failure process. From a simple parametric study, the threshold value of the friction coefficient that modifies the failure mechanism from a single plastic shear band at $\theta_{fr} \approx 47^o$ to multiple distributed plastic shear bands at $\theta_{fr} \approx 56^o$ is in the range $0.2 < \mu < 0.4$.

[Figure 6 about here.]

For a relatively high frictional effects, the composite can sustain a relatively high level of strain under transverse compression, typically around 4-5%, justified by the high compressive resistance of the matrix. For low values of $\mu$, the premature failure of the fibre/matrix interface leads to the concentration of plastic strain in a single band inducing the catastrophic failure of the material (see Figure 6). This might be the case in HOT/WET conditions, as the water absorbed by the polymer tends to form micro channels around the fibers reducing the friction coefficient [43, 44]. In the absence of more reliable data, the friction coefficient in HOT/WET conditions was set to $\mu = 0.01$ leading to failure initiating at the fibre/matrix interface followed by shear banding at $\theta_{fr} \approx 47^o$, as shown in Figure 7.

[Figure 7 about here.]

When pure shear loading is applied to the RVE, different behaviors are found depending on the shearing direction, parallel or perpendicular to the fibers. If shear is applied parallel to the fibers ($\tau_{\parallel}$), the failure mechanism is dominated by interfacial decohesion or by matrix yielding, depending on the interface strength [45]. In the particular case of the AS4/8552 material studied in this work, the interface strength is slightly lower than the matrix shear limit. Thus, fracture is triggered by interface debonding rather than by matrix plasticity, similarly to the pure transverse tension case. As the interface debonds, the matrix holds progressively shear loads and plastic band deformations

are formed. On the other hand, if shear is applied in the plane perpendicular to the fibers ($\tau_{\perp}$), the deformation pattern after matrix yielding is different. Once interface debonding initiates, fiber rotation starts resulting in a gradually stiffer response of the composite material. The in-plane shear response of the composite lamina ($\tau_{12}$) was approximated in this work by averaging the values obtained along the fibers $\tau_{\parallel}$ and perpendicular to the fibers $\tau_{\perp}$, as suggested by Totry et al. [45].

The values of the elastic constants (transverse elastic modulus and in-plane shear modulus) as well as the predictions of the transverse tensile strength, transverse compressive strength and in-plane shear strength for a AS4/8552 lamina are gathered in Table 3. The reported numerical results are the average of five different random realizations and are in good agreement with experimentally-obtained average ply properties reported in the literature [15], specially for RT/DRY conditions.

[Table 3 about here.]

*4.2. Failure envelopes*

One of the potential applications of computational micromechanics is the prediction of ply failure envelopes, i.e. the failure loci for the whole range of combined stress states. In this work the focus is put on the prediction of the intersection of the failure envelope with the $\sigma_{22} - \tau_{12}$ stress plane. This is carried by applying different combinations of transverse and in-plane shear loads, as represented in Figure 8 for RT/DRY and HOT/WET conditions. The numerical results are compared to the predictions of physically-based Puck ply failure criteria [8] using as model inputs the AS4/8552 material properties available in literature [15] and summarized in Table 3.

[Figure 8 about here.]

The effect of friction between fibres and matrix is clearly visible on the shape of the failure envelopes mainly on the transverse compression quadrant. The results reported in this work suggest that fiber/matrix friction controls the transition between interface-dominated failure in pure shear loading to matrix-dominated failure for pure compression loading. Shear hardening under moderate transverse compression has been observed experimentally (e.g. [42]) and is predicted by Puck's criteria [8]. If fibre/matrix friction is omitted, or the friction coefficient is low, no change in the failure mechanism is obtained and no shear hardening is predicted by computational micromechanics as reported in other works [5, 46]. Other authors assumed an arbitrarily large fiber/matrix interface strength in order to capture this effect [3] leading to unrealistic predictions of the in-plane and transverse tension strengths. The results of a parametric analysis of the effect of the friction

coefficient on the shape of the failure envelope for the RT/DRY conditions are shown in Figure 9a. There is a threshold value of the friction coefficient in the range $0.2 < \mu < 0.4$ that triggers the transition of the fracture mechanism. Increasing $\mu$ above this value leads to no significant change in the material response except for the increase in the slope of the shear hardening curve.

[Figure 9 about here.]

The transition between interface-dominated shear failure to matrix-dominated occurs when the interface shear strength, including the friction effects, overcomes the matrix shear strength. As failure of the matrix under compression loading starts to dominate the ply failure process, the fracture angle also starts to change from $\theta_{fr} = 0^o$ to approach a typical shear fracture. Figure 10 shows how that transition is produced in the $\sigma_{22} - \tau_{12}$ frame with increasing ratios of transverse compression over shear loads.

[Figure 10 about here.]

This whole range of processes of ply fracture under transverse compression ($\sigma_{22} < 0$) can be described by a single criterion from the set of Puck failure criteria for plane stress cases [8]:

$$\left(\frac{\tau_T}{S^T - \eta^T \sigma_n}\right)^2 + \left(\frac{\tau_L}{S^L - \eta^L \sigma_n}\right)^2 = 1 \tag{6}$$

wherein the tractions on a possible fracture plane with angle $\theta$ are obtained from the components of the stress tensor defined in the material coordinate system (see Figure 11) as:

$$\begin{aligned} \sigma_n &= \sigma_{22} \cos^2 \theta \\ \tau_T &= -\sigma_{22} \sin \theta \cos \theta \\ \tau_L &= \tau_{12} \cos \theta \end{aligned} \tag{7}$$

$S^L$ and $S^T$ are, respectively, the material shear strengths in fibre and transverse-to-fibre directions while $\eta^L$ and $\eta^T$ are the corresponding internal friction coefficients acting on the fracture plane. The prediction of the correct $\theta_{fr}$ for each biaxial load ratio requires the criterion to be maximised for the whole range of possible fracture angles. Following this procedure will dictate that the fracture angle evolves from $\theta_{fr} = 0^o$, for transverse tension and moderate transverse compression, to $\theta_{fr} \approx 53^o$ for pure transverse compression. A remarkably similar trend is suggested by the computational micromechanical results presented above and by experimental observations [42], with sensible differences being that the increase of $\theta$ predicted by Equation 6 is continuous and progressive up to

$\theta_{fr} \approx 53^o$ while in micromechanics the increase is in discrete steps and up to $\theta_{fr} \approx 56^o$, a value that matches experimental observations [42] more accurately. These differences are likely to be related to the discreetness of the microstructure which is not taken into account in the ply failure model.

[Figure 11 about here.]

The effect of friction on ply failure for transverse compression is also taken into account in Puck's criterion wherein the shear strengths are affected, i.e. increased, by negative normal tractions acting on the fracture plane on $\eta^L$ and $\eta^T$ proportions (note that Equation 6 is only valid for $\sigma_{22} < 0$). For $\theta = 0^o$, $\eta^L$ defines the slope of the shear hardening region in the failure envelope. A linear interpolation of the micromechanical simulations in this range, for a fibre-matrix friction coefficient of $\mu = 0.4$, results in $\eta^L = 0.22$ (see Figure 9a), a value close to the one experimentally observed by Koerber et al. [42] ($\eta^L = 0.26$) for a similar CFRP system (IM7/8552). Given these correlations, the parametrically-obtained friction coefficient $\mu = 0.4$ is adopted at this point and used in the following predictions.

For a HOT/WET environment, ply fracture seems to be controlled by interface failure in the whole range of transverse biaxial loads. Hence, no shear hardening should be observed in moderate compression. As the drop of friction coefficient due to water uptake is not perfectly defined, two failure envelopes, corresponding to $\mu = 0.01$ and $\mu = 0.4$, are represented in Figure 8 in order to establish lower and upper bounds for the failure envelope for HOT/WET conditions.

Given the importance of the hydrostatic pressure in the behavior of polymers and the uncertainty about the model parameters that control its effect, namely the internal friction angle, a parametric study on the variation of this parameter on the behaviour of the composite was carried out. The internal friction angle ($\beta$) is related to the coefficient of the hydrostatic term of constitutive equation of the epoxy matrix (Equation 1) and its variation implies a change in the material biaxial compressive response (Equation 3). The influence of the polymer matrix plastic behaviour in the global composite microstructure can be assessed by comparing three failure envelopes corresponding to values of $\beta = 22^o$, $29^o$ and $36^o$ and a fixed value of the friction coefficient ($\mu = 0.4$), as shown in Figure 9b. The curve for $\beta = 29^o$ corresponds to the material properties gathered in Table 1 and represents the baseline configuration. The other values considered herein represent a lower and upper bound for most of epoxy resins [29].

As observed in Figure 9b, the material pure transverse compressive strength ($Y_C$) and the slope of the shear hardening curve ($\eta^L$) increase for $\beta = 22^o$. However, this effect is not symmetric, i.e.

$Y_C$ and $\eta^L$ do not significantly decrease for an equivalent increase of $\beta$ to $36^o$. In addition, the ply fracture angle for pure transverse compression ($\theta_{fr}$) is kept constant regardless the internal friction angle of the polymer, as shown in Figure 12. It appears that decreasing $\beta$ from the baseline value of $29^o$ results in a pronounced increase of the matrix yield load with a direct effect on $Y_C$. Indirectly, a stronger matrix allows the increase of the normal stresses on the fiber/matrix interface and, as a consequence of friction, an increase on its shear resistance. In other words, decreasing the friction angle of the polymer increases its compressive strength [29] and hence of the friction shear load transferred between the fibers and the polymer. On the other hand, increasing $\beta$ above $29^o$ appears not to have a significant impact on matrix compressive yielding and neither on $\eta^L$, i.e. the effect of this parameter is nonlinear. Hence, in the absence of more objective information, a value of $\beta \approx 29^o$ seems to be appropriate to characterize the 8552 epoxy resin behaviour as it results in values of $Y_C$, $\eta^L$ and $\theta_{fr}$ coherent with experimental data.

The results and correlations made in this section lead to the hypotheses that $\eta^L$ may be regarded as a ply-homogenized combination of the effects of fibre/matrix interface friction and matrix internal friction, while $\eta^T$ would better correspond to matrix internal friction only. The confirmation of these hypotheses would require further investigation.

[Figure 12 about here.]

## 5. Conclusions

In this work, the transverse tensile strength, transverse compressive strength and in-plane shear strength of a unidirectional AS4/8552 lamina under both RT/DRY and HOT/WET environmental conditions have been determined using computational micromechanics. The main parameters of the constitutive equations of the microconstituents, including the fiber/matrix interface and polymer plastic behavior, were obtained experimentally by means of *in-situ* nano-indentation tests. Using only micromechanical properties, the model reproduces the ply stress-train behavior and fracture mechanisms observed experimentally [17, 23, 45], both for uniaxial and biaxial stress states. Hence, this paper suggests that virtual ply characterization tests, based on reliable properties of the micro-constituents, can replace the physical experiments, at least for material screening purposes. These virtual tests provide full control of the composite microstructure and constituent properties, allowing microstructural optimization to be performed in the future [47]. Moreover, complex stress states, not possible to be applied experimentally, can be simulated. Finally, this work shows that

there is a need to improve existing ply failure criteria that rely only on ply properties [8, 9]. Without exception, these assume microstructures containing perfect fiber-matrix bonding and do not take into account important micromechanical parameters such as fibre/matrix interface strength and interface friction.

## Acknowledgments

The authors would like to acknowledge the support provided by AIRBUS SAS through the project SIMSCREEN (Simulation for Screening Composite Materials Properties). Additionally, C.S. Lopes acknowledges the support of the Spanish Ministry of Economy and Competitiveness through the *Ramón y Cajal* program. The help of Dr. Miguel Monclús and Dr. Jon Molina in the experimental work is also gratefully acknowledged.

## References

## References

[1] M. Hinton, A. Kaddour, P. Soden, A further assessment of the predictive capabilities of current failure theories for composite laminates: comparison with experimental evidence, Composites Science and Technology 64 (2004) 549–588.

[2] I. M. Daniel, J.-J. Luo, P. M. Schubel, B. T. Werner, Interfiber/interlaminar failure of composites under multi-axial states of stress, Composites Science and Technology 69 (2009) 764–771.

[3] E. Totry, C. González, J. LLorca, Failure locus of fiber-reinforced composites under transverse compression and out-of-plane shear, Composites Science and Technology 68 (2008) 829–839.

[4] M. Romanowicz, A numerical approach for predicting the failure locus of fiber reinforced composites under combined transverse compression and axial tension, Computational Materials Science 51 (2012) 7–12.

[5] A. Melro, P. Camanho, F. Andrade Pires, S. T. Pinho, Micromechanical analysis of polymer composites reinforced by unidirectional fibres: Part II ??? Micromechanical analyses, International Journal of Solids and Structures 50 (2013) 1906–1915.

[6] L. P. Canal, C. González, J. Segurado, J. LLorca, Intraply fracture of fiber-reinforced composites: Microscopic mechanisms and modeling, Composites Science and Technology 72 (2012) 1223–1232.

[7] J. LLorca, C. González, J. M. Molina-Aldareguía, J. Segurado, R. Seltzer, F. Sket, M. Rodríguez, S. Sádaba, R. Muñoz, L. P. Canal, Multiscale modeling of composite materials: a roadmap towards virtual testing., Advanced materials 23 (2011) 5130–47.

[8] A. Puck, H. Schürmann, Failure analysis of FRP laminates by means of physically based phenomenological models, Composites Science and Technology 62 (2002) 1633–1662.

[9] C. Davila, P. Camanho, C. A. Rose, Failure Criteria for FRP Laminates, Journal of Composite Materials 39 (2005) 323–345.

[10] G. Catalanotti, P. P. Camanho, A. Marques, Three-dimensional failure criteria for fiber-reinforced laminates, Composite Structures 95 (2013) 63–79.

[11] J. Segurado, J. LLorca, A numerical approximation to the elastic properties of sphere-reinforced composites, Journal of the Mechanics and Physics of Solids 50 (2002) 2107–2121.

[12] T. Vaughan, C. McCarthy, A combined experimental???numerical approach for generating statistically equivalent fibre distributions for high strength laminated composite materials, Composites Science and Technology 70 (2010) 291–297.

[13] S. T. Pinho, L. Iannucci, P. Robinson, Physically based failure models and criteria for laminated fibre-reinforced composites with emphasis on fibre kinking. Part II: FE implementation, Composites Part A Applied Science and Manufacturing 37 (2006) 766–777.

[14] A. Melro, P. Camanho, F. Andrade Pires, S. T. Pinho, Micromechanical analysis of polymer composites reinforced by unidirectional fibres: Part I ??? Constitutive modelling, International Journal of Solids and Structures 50 (2013) 1897–1905.

[15] K. Marlett, Y. Ng, J. Tomblin, E. Hooper, NCAMP Test Report: CAM-RP-2010-002 Rev A, Technical Report, National Institute for Aviation Research, 2011.

[16] C. Lopes, S. Sádaba, C. González, J. LLorca, P. Camanho, Physically-Sound Simulation of Low-Velocity Impact on Fibre Reinforced Laminates, International Journal of Impact Engineering (2015) 1–15.

[17] C. González, J. LLorca, Mechanical behavior of unidirectional fiber-reinforced polymers under transverse compression: Microscopic mechanisms and modeling, Composites Science and Technology 67 (2007) 2795–2806.

[18] D. Trias, J. Costa, a. Turon, J. E. Hurtado, Determination of the critical size of a statistical representative volume element (SRVE) for carbon reinforced polymers, Acta Materialia 54 (2006) 3471–3484.

[19] A. R. Melro, P. P. Camanho, S. T. Pinho, Generation of random distribution of fibres in long-fibre reinforced composites, Composites Science and Technology 68 (2008) 2092–2102.

[20] Dassault Systèmes, Abaqus 6.13 Documentation, 2013.

[21] L. Yang, Y. Yan, Y. Liu, Z. Ran, Microscopic failure mechanisms of fiber-reinforced polymer composites under transverse tension and compression, Composites Science and Technology 72 (2012) 1818–1825.

[22] D. Ashouri Vajari, C. González, J. Llorca, B. N. Legarth, A numerical study of the influence of microvoids in the transverse mechanical response of unidirectional composites, Composites Science and Technology 97 (2014) 46–54.

[23] L. P. Canal, J. Segurado, J. LLorca, Failure surface of epoxy-modified fiber-reinforced composites under transverse tension and out-of-plane shear, International Journal of Solids and Structures 46 (2009) 2265–2274.

[24] B. Fiedler, M. Hojo, S. Ochiai, K. Schulte, M. Ando, Failure behavior of an epoxy matrix under different kinds of static loading, Composites Science and Technology 61 (2001) 1615–1624.

[25] D. C. Drucker, W. Prager, Soil mechanics and plastic analysis for limit design, Quarterly of Applied Mathematics 10 (1952) 157–165.

[26] J. Lubliner, J. Oliver, S. Oller, E. Oñate, A plastic-damage model for concrete, International Journal of Solids and Structures 25 (1989) 299–326.

[27] J. Lee, G. L. Fenves, Plastic-Damage Model for Cyclic Loading of Concrete Structures, Journal of Engineering Mechanics 124 (1998) 892–900.

[28] L. P. Canal, C. González, J. M. Molina-Aldareguía, J. Segurado, J. LLorca, Application of digital image correlation at the microscale in fiber-reinforced composites, Composites Part A: Applied Science and Manufacturing 43 (2012) 1630–1638.

[29] M. Rodríguez, J. M. Molina-Aldareguía, C. González, J. LLorca, Determination of the mechanical properties of amorphous materials through instrumented nanoindentation, Acta Materialia 60 (2012) 3953–3964.

[30] A. Turon, P. Camanho, J. Costa, C. Dávila, A damage model for the simulation of delamination in advanced composites under variable-mode loading, Mechanics of Materials 38 (2006) 1072–1089.

[31] M. L. Benzeggagh, M. Kenane, Measurement of mixed-mode delamination fracture toughness of unidirectional glass/epoxy composites with mixed-mode bending apparatus, Composites Science and Technology 56 (1996) 439–449.

[32] G. Alfano, E. Sacco, Combining interface damage and friction in a cohesive-zone model, International Journal for Numerical Methods in Engineering 68 (2006) 542–582.

[33] I. Guiamatsia, G. D. Nguyen, A thermodynamics-based cohesive model for interface debonding and friction, International Journal of Solids and Structures 51 (2014) 647–659.

[34] M. Rodríguez, J. M. Molina-Aldareguía, C. González, J. LLorca, A methodology to measure the interface shear strength by means of the fiber push-in test, Composites Science and Technology 72 (2012) 1924–1932.

[35] C. Chamis, Mechanics of Composite Materials: Past, Present, and Future, ASTM 11 (1989).

[36] Beuth, DIN EN 2823 - Aerospace series - Fibre reinforced plastics - Determination of the effect of exposure to humid atmosphere on physical and mechanical characteristics, 1999.

[37] W. Oliver, G. Pharr, An improved technique for determining hardness and elastic modulus using load and displacement sensing indentation experiments, Journal of Materials Research 7 (1992) 1564–1583.

[38] M. Herráez, D. Mora, F. Naya, C. S. Lopes, C. González, J. LLorca, Transverse cracking of cross-ply laminates: A computational micromechanics perspective, Composites Science and Technology 110 (2015) 196–204.

[39] E. H. Andrews, A. Stevenson, Fracture energy of epoxy resin under plane strain conditions, Journal of Materials Science 13 (1978) 1680–1688.

[40] S. Ogihara, J. Koyanagi, Investigation of combined stress state failure criterion for glass fiber/epoxy interface by the cruciform specimen method, Composites Science and Technology 70 (2010) 143–150.

[41] C. González, J. LLorca, Multiscale modeling of fracture in fiber-reinforced composites, Acta Materialia 54 (2006) 4171–4181.

[42] H. Koerber, J. Xavier, P. Camanho, High strain rate characterisation of unidirectional carbon-epoxy IM7-8552 in transverse compression and in-plane shear using digital image correlation, Mechanics of Materials 42 (2010) 1004–1019.

[43] G. Huang, H. Sun, Effect of water absorption on the mechanical properties of glass/polyester composites, Materials and Design 28 (2007) 1647–1650.

[44] J. Wang, B. Chen, N. Liu, G. Han, F. Yan, Combined effects of fiber/matrix interface and water absorption on the tribological behaviors of water-lubricated polytetrafluoroethylene-based composites reinforced with carbon and basalt fibers, Composites Part A: Applied Science and Manufacturing 59 (2014) 85–92.

[45] E. Totry, J. M. Molina-Aldareguía, C. González, J. LLorca, Effect of fiber, matrix and interface properties on the in-plane shear deformation of carbon-fiber reinforced composites, Composites Science and Technology 70 (2010) 970–980.

[46] P. P. Camanho, a. Arteiro, a. R. Melro, G. Catalanotti, M. Vogler, Three-dimensional invariant-based failure criteria for fibre-reinforced composites, International Journal of Solids and Structures 55 (2014) 92–107.

[47] M. Herráez, C. González, C. S. Lopes, R. Guzmán de Villoria, J. Llorca, T. Varela, J. Sánchez, Computational micromechanics evaluation of the effect of fibre shape on the transverse strength of unidirectional composites: an approach to virtual materials design, Submitted to Composites Part A: Applied Science and Manufacturing (2015).

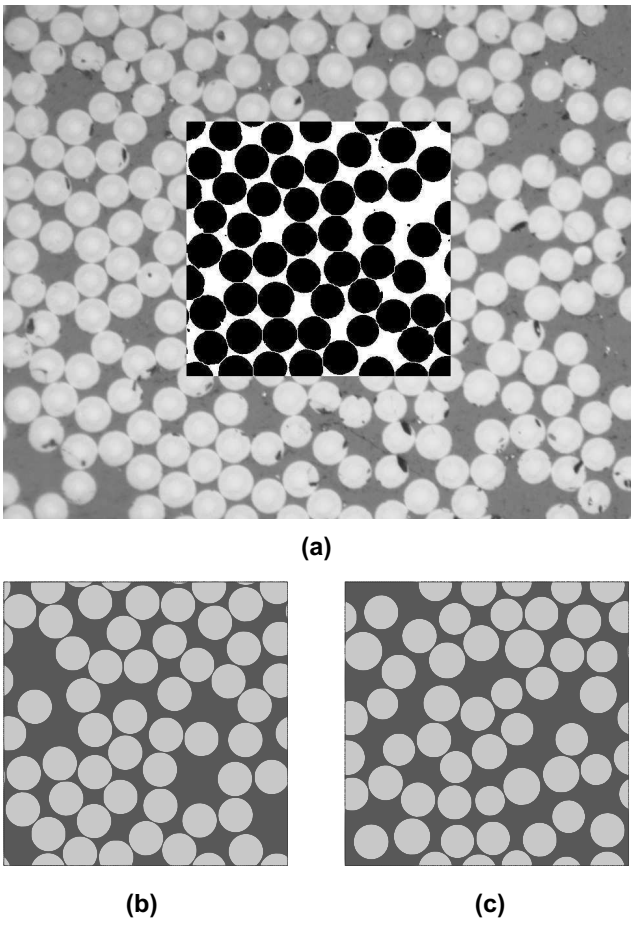


Figure 1: (a) AS4/8552 cross-section micrograph.(b) NNA virtual microstructure.(c) RSA virtual microstructure

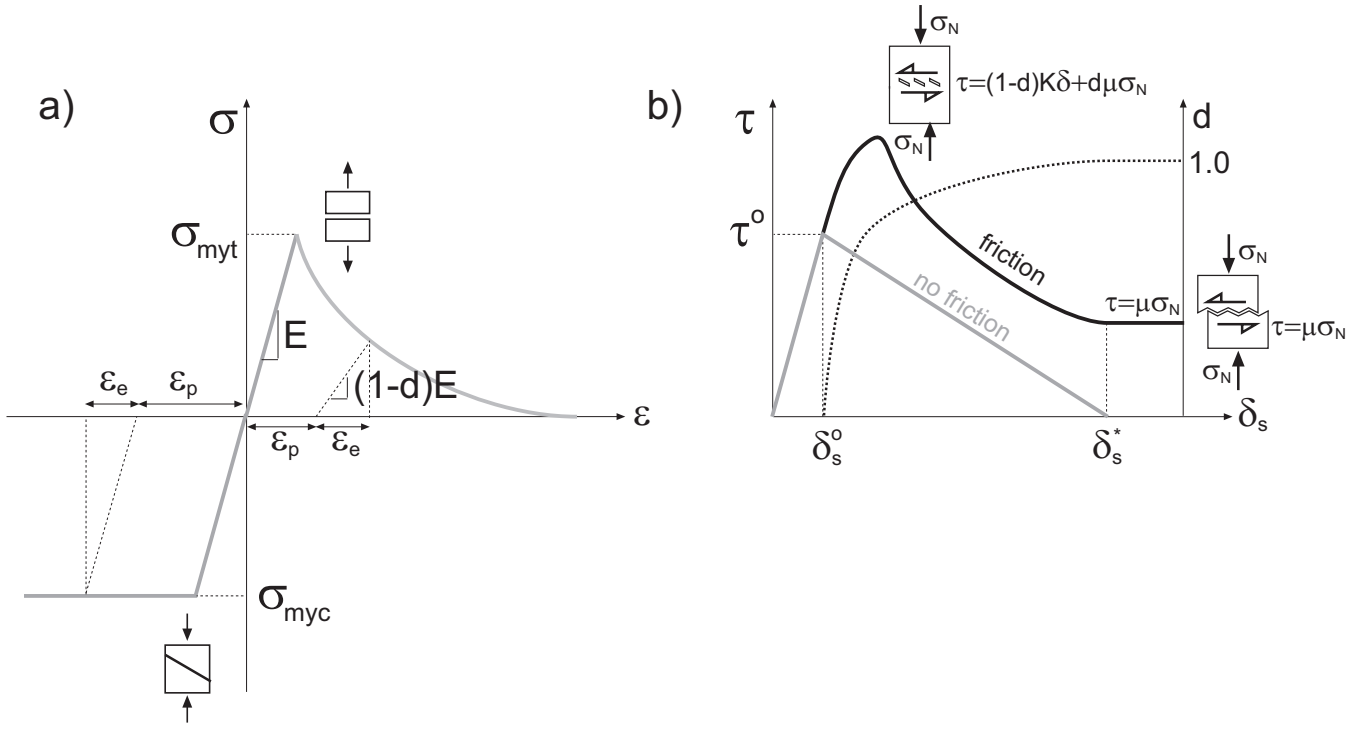


Figure 2: a) Schematic of the uniaxial tensioncompression response of the epoxy matrix according to the damage-plasticity model for quasi-brittle materials, b) Schematics of the shear response of the damage-friction model for fiber/matrix interfaces.

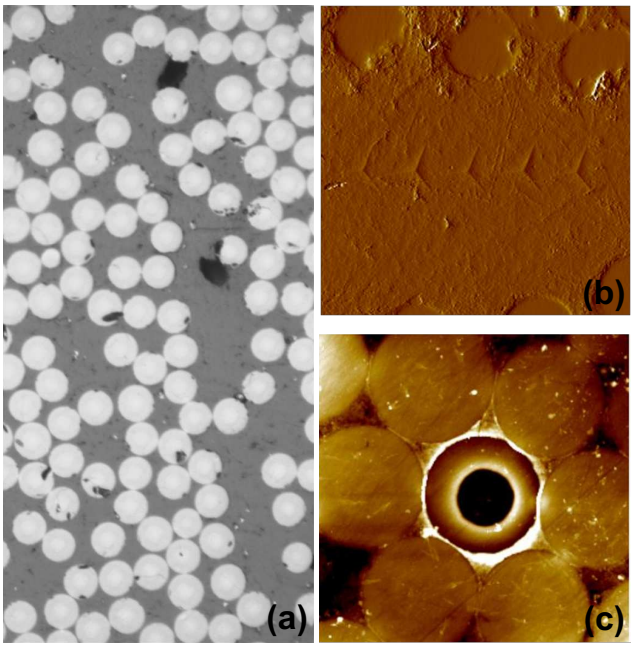


Figure 3: Micromechanical tests.(a) AS4/8552 cross section showing matrix rich regions. Atomic Force Microscope (AFM) image showing (b) the Berkovich pyramidal indenter footprint on a polymer matrix and (c) the flat punch tip footprint on a carbon fiber

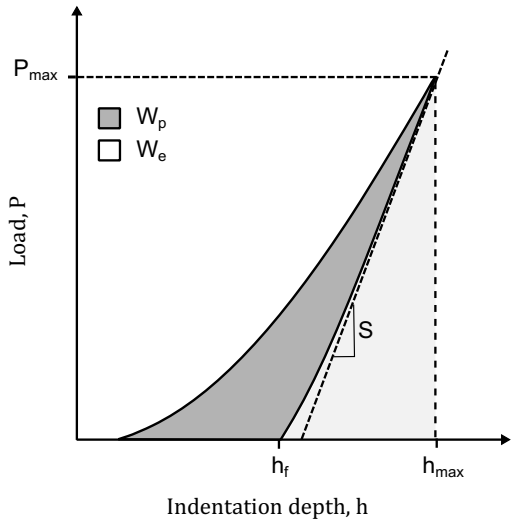


Figure 4: Typical load-displacement curve resulting from the nanoindentation test (adapted from [29])

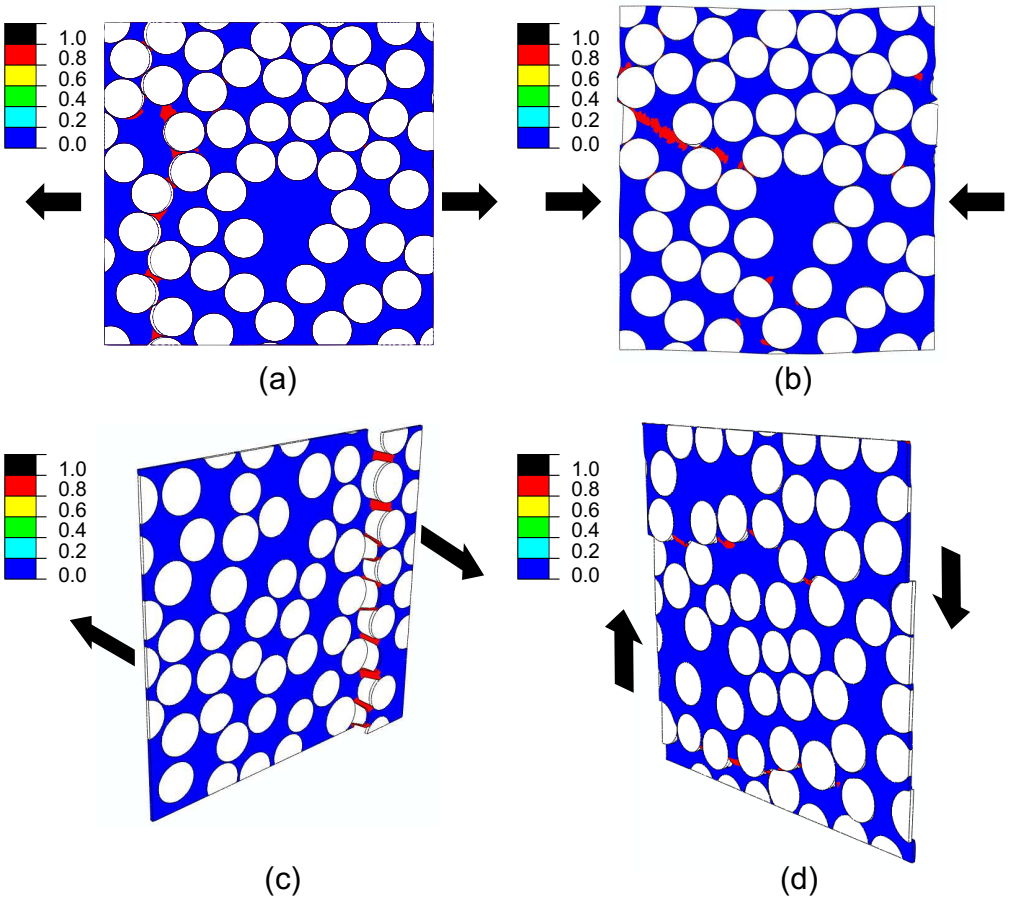


Figure 5: Predicted failure modes in a AS4/8552 ply. Tensile damage for transverse tension (a), parallel shear (c) and perpendicular shear (d). Compression damage for transverse compression (b)

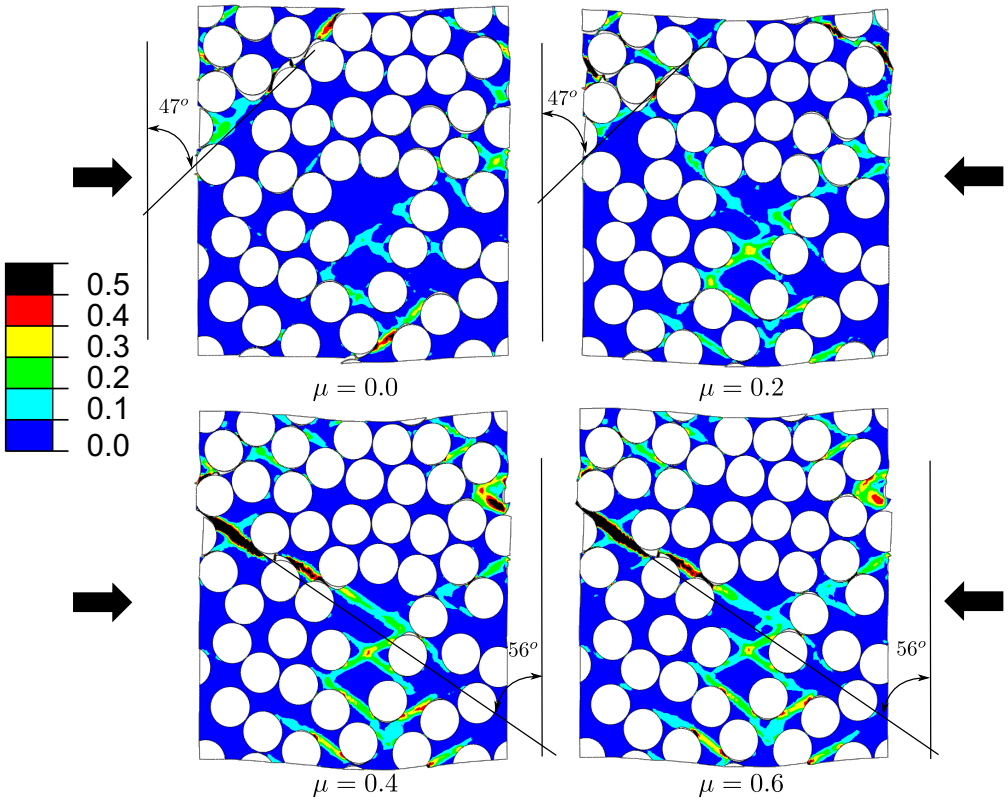


Figure 6: Effect of the friction coefficient, $\mu$, in the transverse compression loading when $\epsilon = 5\%$. Prediction of accumulated plastic strain (PEEQ)

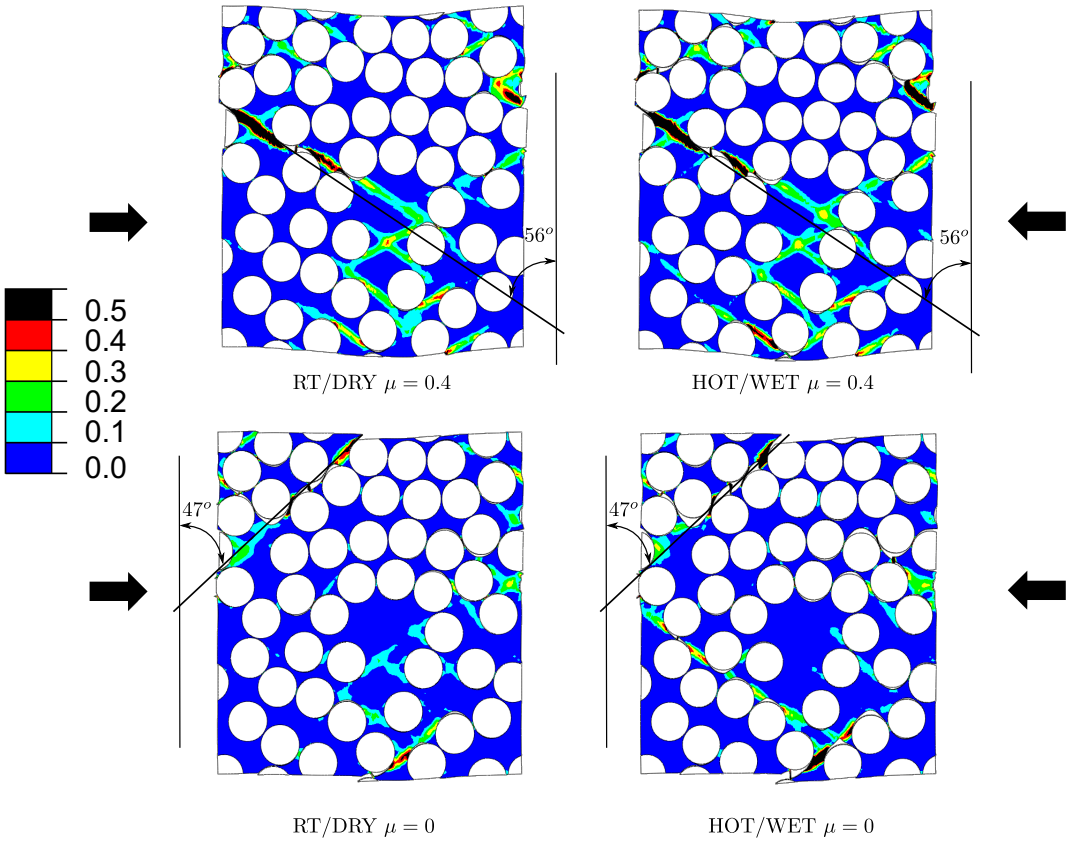


Figure 7: Effect of the environmental conditions in the transverse compression loading. Predicted accumulated plastic strain (PEEQ) at $\epsilon = 5.5\%$ for $\mu = 0.4$ and $\mu = 0.0$ under RT/DRY environment. Predicted accumulated plastic strain (PEEQ) at $\epsilon = 4.8\%$ for $\mu = 0.4$ and $\mu = 0.0$ under HOT/WET environment

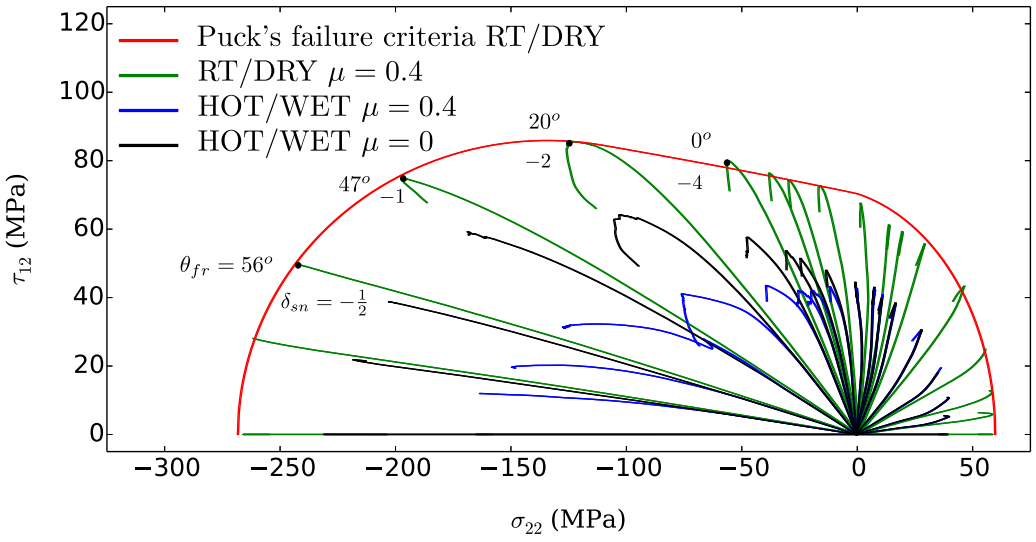


Figure 8: Predicted failure locus in a AS4/8552 ply under combined transverse stress and in-plane shear for RT/DRY and HOT/WET conditions(with and without friction)

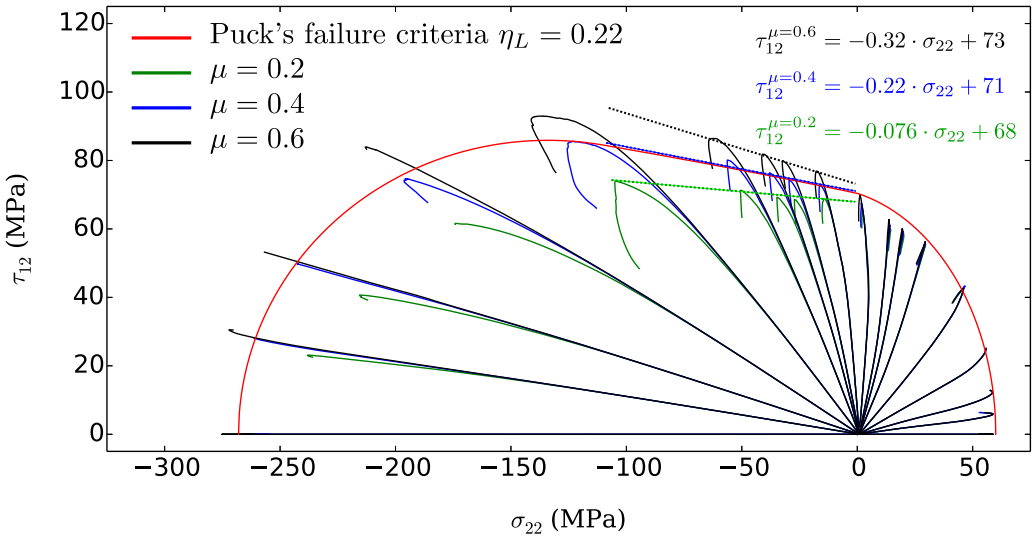


(a)

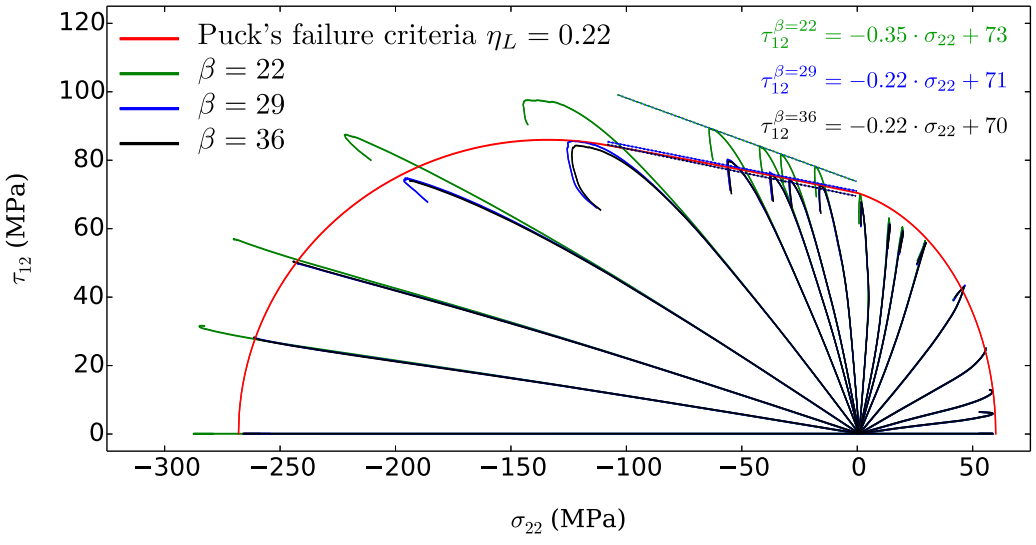


(b)

Figure 9: Effect of model parameters on the predicted failure locus in a AS4/8552 ply under combined transverse stress and in-plane shear: a) Effect of the friction coefficient between fiber and matrix; b) Effect of polymer matrix internal friction angle.

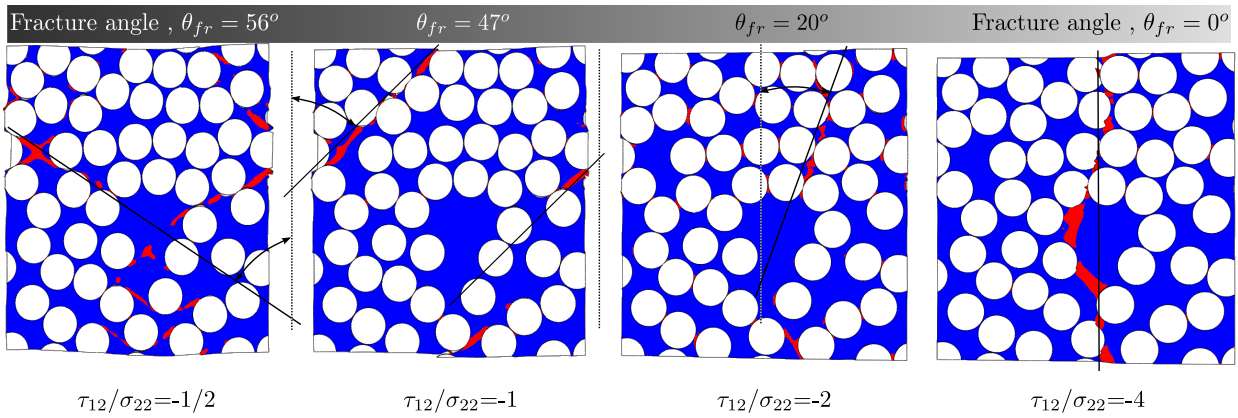


Figure 10: Predicted fracture angles for different load combinations and RT/DRY conditions($\mu = 0.4$). The image show the concentration of accumulated plastic strain (PEEQ) for the different biaxial loading states

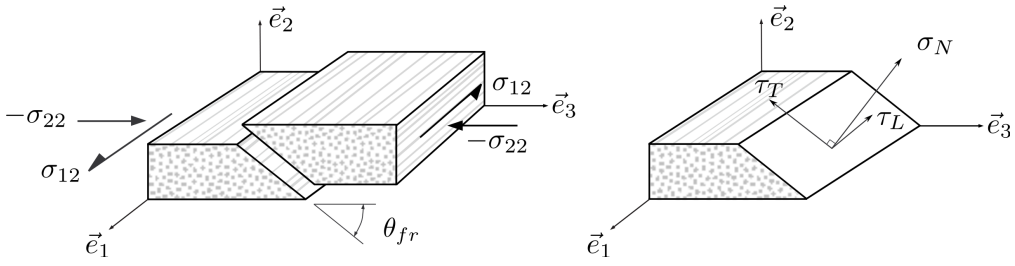


Figure 11: a) Fracture plane for a ply subjected to transverse compression and in-plane shear; b) Stresses in the fracture plane.

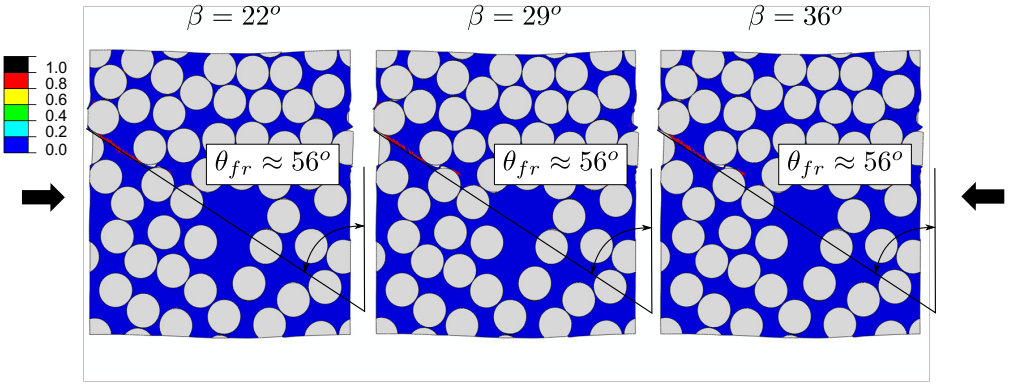


Figure 12: Predicted compression damage and fracture angle in a AS4/8552 ply under a pure transverse compressive stress state for different polymer matrix internal friction angles, $\beta$

Table 1: Properties of the AS4/8552 material constituents used in the FE simulations. Polymer fracture energy, tensile strength, Poisson ratio and internal friction angle are taken from [38]. Carbon fiber elastic properties are also extracted from [38]

| AS4 carbon fiber properties | | | | | | | |
|---|---|---|---|---|---|---|---|
| | $E_{f1}(GPa)$ | $E_{f2}(GPa)$ | $G_{f12}(GPa)$ | $G_{f23}(GPa)$ | $\nu_{f12}$ | $\alpha_{f1}(K^{-1})$ | $\alpha_{f2}(K^{-1})$ |
| | 231 | 12.97 | 11.28 | 4.45 | 0.3 | -0.9e-6 | 7.2e-6 |
| 8552 epoxy matrix properties | | | | | | | |
| *Condition* | $E_m(GPa)$ | $\nu_m$ | $\sigma_{myt}(MPa)$ | $\beta$ | $\sigma_{myc}(MPa)$ | $\mathcal{G}_m(J/m^2)$ | $\alpha_m(K^{-1})$ |
| RT/DRY | 5.07 | 0.35 | 121 | 29 | 176 | 100 | 52e-6 |
| HOT/WET | 4.28 | 0.35 | 104 | 29 | 152 | 100 | 1.5e-6 |
| AS4/8552 fibre/matrix interface properties | | | | | | | |
| Condition | $\sigma_N(MPa)$ | $\tau_T(MPa)$ | $\tau_L(MPa)$ | $\mathcal{G}_{Ic}(J/m^2)$ | $\mathcal{G}_{IIc}(J/m^2)$ | $\mathcal{G}_{IIIc}(J/m^2)$ | |
| RT/DRY | 42 | 64 | 64 | 2 | 100 | 100 | |
| HOT/WET | 30 | 45 | 45 | 2 | 100 | 100 | |

Table 2: 8552 epoxy resin indentation and AS4/8552 interface push-in tests results under RT/DRY and HOT/WET (70C/85%) conditions

| Condition | $\beta(^o)$ | $\sigma_{myc}(MPa)$ | $E(GPa)$ | $\tau_d(MPa)$ |
|---|---|---|---|---|
| RT/DRY | 29 | 176 ± 17 | 5.07 ± 0.3 | 63.77 ± 2.64 |
| HOT/WET | 29 | 152 ± 08 | 4.28 ± 0.2 | 44.55 ± 2.72 |

Table 3: Numerically-predicted vs. experimentally-obtained elastic constants, transverse and shear strengths for a AS4/8552 ply (ply thickness $t$=0.184mm)

| | RT/DRY | | HOT/WET | |
|---|---|---|---|---|
| Property | Micromechanics | Literature [15] | Micromechanics | Literature [15] |
| $E_2$(GPa) | 9.2 | 9.6 | 8.3 | 8.4 |
| $G_{12}$(GPa) | 4.8 | 4.8 | 3.1 | 2.3 |
| $Y_T$(MPa) | 61±3 | 63.9 | 36±2 | 24.1 |
| $Y_C$(MPa) | 290±30 | 268.0 | 141±7 | 136.0 |
| $S_L^{0.2\%}$(MPa) | 55±1 | 55.2 | 34±1 | 23.2 |
| $S_L^{5\%}$(MPa) | 88±3 | 91.6 | 55±3 | 38.0 |